Materialia 16 (2021) 101068

Contents lists available at ScienceDirect

Materialia

journal homepage: www.elsevier.com/locate/mtla

Grain growth of nanocrystalline aluminum under tensile deformation: A combined *in situ* TEM and atomistic study

Sandra Stangebye[a], Yin Zhang[b], Saurabh Gupta[b], Ehsan Hosseinian[b], Frank Yu[a], Christopher Barr[c], Khalid Hattar[c], Olivier Pierron[b], Ting Zhu[b], Josh Kacher[a,*]

[a] School of Materials Science Engineering, Georgia Institute of Technology, Atlanta, GA 30332, United States
[b] Woodruff School of Mechanical Engineering, Georgia Institute of Technology, Atlanta, GA 30332, United States
[c] Sandia National Laboratories, Albuquerque, NM 87185, United States

ABSTRACT

Nanocrystalline Al thin films have been strained *in situ* in a transmission electron microscope using two separate nanomechanical techniques involving a push-to-pull device and a microelectromechanical system (MEMS) device. Deformation-induced grain growth was observed to occur via stress-assisted grain boundary migration with extensive grain growth occurring in the necked region, indicating that the increase in local stress drives the boundary migration. Under applied tensile stresses close to the ultimate tensile strength of 450 MPa for a nanocrystalline Al specimen, measured boundary migration speeds are 0.2 – 0.7 nm s^{-1} for grains outside necked region and increases to 2.5 nm s^{-1} for grains within the necked region where the local estimated tensile stresses are elevated to around 630 MPa. By tracking grain boundary motion over time, molecular dynamics simulations showed qualitative agreement in terms of pronounced grain boundary migration with the experimental observations. The combined *in situ* observation and molecular dynamics simulation results underscore the important role of stress-driven grain growth in plastically deforming nanocrystalline metals, leading to intergranular fracture through predominant grain boundary sliding in regions with large localized deformation.

1. Introduction

Nanocrystalline (nc) and ultrafine-grained (ufg) metals exhibit a wealth of physical behaviors different from their coarse-grained counterparts, such as increased yield strength, enhanced diffusivity, and higher specific heat capacity and coefficient of thermal expansion [1]. These differences, most notably the increase in strength, make nanostructured metals an attractive candidate for materials used in next-generation micro- and nanoscale devices, such as microelectromechanical system (MEMS) devices. However, a thorough understanding of the deformation mechanism determining their mechanical properties is required before widespread application of nanostructured metals.

The superior strength of nc and ufg metals is attributed to the well-known Hall-Petch relationship, which states that yield strength scales inversely with grain size [2,3]. This relationship has been observed for a wide variety of nanostructured metals manufactured using different processing techniques [4,5]. Within the ufg regime (grain sizes (d) ranging from 1 μm down to 100 nm), the proposed rate-controlling mechanism is the interaction of intragranular dislocations generated at grain boundaries (GB) [6], with the increased number of GBs impeding further dislocation glide, essentially serving as obstacles to plastic deformation [7]. However, as the grain size is decreased past $d < 20$ nm, the direct benefit of this is lost due to the transition to GB-dominated deformation processes. Theoretically, this transition has been linked to a critical grain size where an individual grain is no longer capable of effectively storing a single dislocation, resulting in an 'inverse' Hall-Petch effect [8]. In this regime, molecular dynamic (MD) simulations have predicted that the deformation is dominated by GB processes, such as GB sliding [6,9,10].

Deformation mechanisms within the nc regime, prior to the inverse Hall-Petch effect ($\sim$20 nm $< d <$ 100 nm), exhibit a mixture of both dislocation and GB-mediated processes, with several proposed mechanisms including GB sliding [6], dislocation emission and absorption at GBs [11,12], grain rotation [13–16], GB migration, and diffusional creep [17]. Recent studies have also shown that room temperature grain coarsening can largely influence the mechanical properties of nc Al. Reports of discontinuous grain growth in nc Al leading to increased ductility indicate that grain growth early in plastic deformation may be critical in developing stable regions of plasticity [18]. *In situ* TEM straining of nc Al has shown fast GB-migration near a crack tip prior to dislocation activity [19]. GB migration was seen to occur in a discontinuous 'jerky' fashion with measured GB migration velocity ranging from 0.1 – 0.2 nm s^{-1} up to 200 nm s^{-1} for the collapsing of small grains. The varying growth rates is indicative of different mechanisms of GB migration, with the fastest velocity indicating the limited stability of the smallest of grains. Another study has reported a fivefold increase in grain size in the immediate vicinity of an indenter tip during *in situ* TEM nanoindentation, with the coarsening halting once grains are large enough to accommodate dislocation mechanisms [20]. In each of the abovementioned experiments, grain growth was observed to occur within regions of increased stress (within gauge section, ahead of crack tip, etc.), sug-

* Corresponding author.
E-mail address: josh.kacher@mse.gatech.edu (J. Kacher).

https://doi.org/10.1016/j.mtla.2021.101068
Received 2 November 2020; Accepted 6 March 2021
Available online 10 April 2021
2589-1529/© 2021 Acta Materialia Inc. Published by Elsevier B.V. All rights reserved.

gesting that GB migration is sensitive to the local stress state. Results by Rupert et al., where nc Al thin films were deformed with different geometric concentrations in order to induce spatial variations in the stress and strain states, further reinforce this finding [21]. Not only was it determined that the stress induced grain growth, but they were further able to separate the effect of normal vs. shear stress, finding that the most severe grain growth was measured in a region with the highest distortional energy due to shear stresses.

These results point to stress-assisted GB migration leading to grain growth in nc Al [18,21,22]. The mechanisms for stress-assisted GB migration have been investigated for low-angle tilt GBs, where the GB structure is simply described as a discrete network of dislocations [23]. Under shear stress, the glide of edge dislocations out of the original GB plane can result in coupled sliding and migration of the GB [24,25]. This mechanism is not assumed to operate for a high-angle GB since the boundary can no longer be described as a simple array of dislocations. However, MD simulations [24,26] and experiments on bi-crystals [27,28] with high-angle tilt boundaries have indicated that the coupled mode of GB sliding and migration is not limited to low-angle boundaries. Cahn et al. showed that the Frank-Bilby equation can accurately describe the dislocation content within high-angle GBs and that forces imposed on these dislocations due to applied shear stress lead to the back-and-forth motion of the GB [29]. However, these simulations are limited to relatively simple tilt GBs which may be uncommon for most real boundaries seen in polycrystals. Alternative proposed mechanism of GB migration involves the nucleation and glide of extrinsic GB dislocations, or disconnections [24,30–32]. The applied shear stress causes the nucleation of a pair of disconnections with opposite Burgers vector and step height sign. The subsequent glide away from each other results in a normal displacement of the GB by an amount equal to the step height. The nucleation of a disconnection is stress driven, but also thermally assisted at finite temperature. The nucleation becomes athermal once a critical stress level is reached. At elevated temperatures (below 800 K), MD simulations [24,29] reveal stop-and-go type boundary motion of GBs as certain critical values of applied shear stress are required to activate the coupling mode with similar jerky motion observed experimentally [33]. In polycrystals, it is likely that the disconnection nucleation events occur at stress concentrators, such as triple junctions and free surfaces [25,34].

Evidence of disconnection-mediated GB migration has been reported by *in situ* TEM experiments by Rajabzadeh et al. where they observed defect motion along GB in response to applied stress in an Al bicrystal and polycrystal [35]. In the bicrystal, the collective glide of multiple GB disconnections, each forming a step, led to the formation of macro-steps in the GB, with the disconnection glide ranging in speed from a few angstroms per second up to 4 μm s^{-1}. A GB migration speed of 10 nm s^{-1} was observed in the polycrystal, with multiple disconnection glide and annihilation leading to the motion of the boundary and triple junction. Very recently, Zhu et al. has shown through *in situ* TEM shear testing the continuous migration of a Σ11(113) coherent GB by way of nucleation and subsequent lateral motion of GB disconnections at a speed of 2.22 nm s^{-1} [34]. The boundary migration was found to be completely reversible upon the reversal of applied load and consistent for boundaries with different characters, such as different misorientation and pre-existing stacking faults or dislocations. They also illustrated that when present, disconnection nucleation occurred at the triple junction.

The above review indicates that decades of research have advanced our fundamental understanding of the role GBs have in the deformation process of nc metals. However, significant challenges remain toward quantitative characterization of GB-mediated deformation processes within real GB networks of nc metals as well as quantitative correlation between these processes and bulk mechanical properties. One of the limitations to widespread use of nc metals is the notable loss of ductility due to a lack of strain hardening which leads to localized deformation [1], and limited uniform elongation [36,37]. The combination of high flow stress and low work hardening in nc metals promotes neck formation, resulting in 'unusable' elongation and reduced tensile ductility. During the neck formation processes, the role of nano-grain coarsening on this behavior is not well understood. The abovementioned studies provide valuable insight into the mechanisms of deformation induced grain growth, but the techniques used are limited in the ability to measure the far-field applied stress while observing deformation processes, and thus cannot accurately correlate the GB-mediated processes with the mechanical properties.

In this work, we investigate the active deformation mechanisms during tensile loading of nc Al thin films using two quantitative MEMS-based *in situ* TEM nanomechanical testing platforms. This approach allows us to measure far field stress values and correlate them with the active GB and dislocation-based deformation mechanisms with the goal of better understanding the deformation processes that dictate the onset of plastic instability and ultimately the mechanical properties of nc Al thin films. To better understand the atomic-scale mechanisms underpinning GB migration, we conduct MD simulations to track GB migration over time. The combined *in situ* observation and MD simulation results underscore the important role of grain growth in large plastic deformation and intergranular fracture of nc Al.

2. Experimental and modeling methods

2.1. Specimen fabrication and characterization

Nc Al thin film specimens of 200 nm thickness were fabricated via electron beam evaporation of Al (99.99% purity) onto a Si substrate, at a pressure of ~10^{-6} Torr and deposition rate of 0.5 Å/s. The specimens were fabricated using the same batch fabrication technique previously used to fabricate Au specimens [38]. The technique involves optical lithography and a lift-off procedure to define rows of dog-bone shaped specimens, with a gauge section of width ~1.5 and length ~20 μm shown in Fig. 1a. The specimens become free-standing after XeF_2 etching of the Si substrate (see Fig. 1b). Following fabrication, the films were annealed at 450 °C for 2 h in a high vacuum oven. Using a micromanipulator, the specimens were detached from the row of specimens, placed onto the MEMS device, and clamped using UV-curable glue (Fig. 1c). Note that the image in Fig. 1c shows a fractured specimen captured post-deformation. For a subset of the samples, the microstructure was characterized before and after deformation using a Nanomegas precession electron diffraction (PED) system to produce Automated Crystal Orientation Mapping (ACOM) analyzed and visualized using the TSL OIM analysis software. Fig. 1d is a pre-deformation orientation map showing that the initial microstructure has no strong out-of-plane texture with most GBs being of the random high-angle type (Fig. 1f). The films have a generally columnar grain structure with an average grain size of 57 ± 30 nm. The grain size distribution is shown in Fig. 1e.

2.2. *In situ* TEM techniques

The first *in situ* TEM tensile tests were conducted on the Al specimens using a commercial push-to-pull (PTP) device coupled with a PI 95 PicoIndenter on a JOEL 2100 TEM with ACOM capabilities operated at 200 kV. This allows for real-time collection of microstructural information, such as grain size and orientation while also recording force and displacement of the nanoindenter punch which is then related to stress and strain of the specimen. The specimens were placed on the device using a micromanipulator welded with Pt (instead of glue). Additional experiments using this set up provided a way to compare the mechanical behavior of the specimens obtained via MEMS-based testing as well as offer additional microstructural information complementing ACOM results.

In situ TEM tensile tests were also performed using a MEMS-based nanomechanical testing technique [39–42], that has been previously used to perform *in situ* TEM investigations on Au thin film specimens with similar geometry [38,43–45]. The MEMS device is composed of a

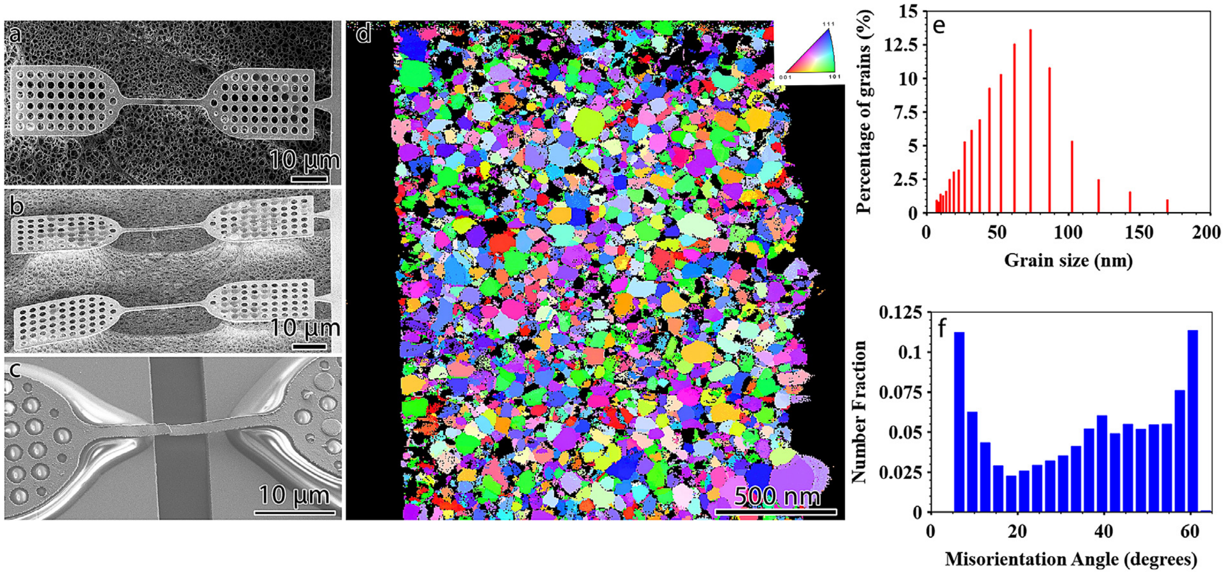

Fig. 1. Sample fabrication and initial microstructure of Al thin film. (a) SEM image of free-standing specimen. (b) Tilted view to show free-standing specimen. (c) SEM image of specimen clamped to MEMS-device using UV-curable epoxy glue. Image is taken at a tilt in order to capture the amount of gauge length that is supported by glue (taken after tensile test to failure). (d) Orientation map showing no out-of-plane texture, (e) corresponding grain size distribution and (f) GB misorientation distribution taken from ACOM data.

thermal actuator, two capacitive sensors, a load sensor beam and a specimen gap in which the thin film specimen is clamped using UV-curable glue. When a voltage is applied, a resulting displacement in the thermal actuator leads to a displacement of the specimen and a shift in capacitive sensors. The change in the two capacitive readings is related to the specimen force and displacement, and thus stress and strain are determined independently. The films were continuously strained in an FEI Tecnai F30 TEM operating at 300 kV at strain rates between $1-3\ \times 10^{-4}\ \mathrm{s}^{-1}$. Radiation damage due to knock on damage imparted by the high energy TEM electrons is a common concern in TEM studies. To mitigate this, most *in situ* TEM experiments are conducted at 200 kV [46]. In this study, grain growth was observed for both 200 and 300 kV accelerating voltages which indicates that the deformation is not influenced by the addition of accelerating voltage from 200 to 300 kV. Snapshots were taken from constant video recording using a Gatan OneView camera, which allowed for direct analysis of entire deformation process. Videos were collected at a frame rate of 20 frames per second with no binning applied. The large size of the camera (16 megapixels) allowed *post mortem* digital magnification of regions of interest. Grain size measurements were completed by manually tracing grains in good contrast and calculating their areas. The grain sizes are reported as equivalent diameters, assuming a circle of the same area.

2.3. MD simulations

MD simulations of uniaxial tension of a nc Al thin film were performed using LAMMPS [47]. The initial thin film structure was constructed by a Voronoi tessellation procedure that generated 32 grains with sizes of about 10 nm, nearly equiaxed shape, and random crystallographic orientations. The thin film structure has dimensions of $32.4 \times 32.4 \times 32.4$ nm and contains a total of 1,996,000 atoms. Periodic boundary conditions were imposed in the tensile loading direction, while other side surfaces are traction free. The interactions between Al atoms were modeled by an embedded atom method (EAM) potential [48]. To relax the GB structures, the system was annealed under zero stress by first heating to 900 K for 100 ps, then cooling to 300 K, and finally equilibrating at 300 K for 10 ps. Uniaxial tensile strain up to 100% was applied with a strain rate of $10^9\ \mathrm{s}^{-1}$ at 300 K.

3. Experimental results

3.1. Overall deformation behavior

In total, six specimens were tested (five with the MEMS-based platform and one with the PTP device). An example of the deformation behavior of one specimen in Fig. 2 shows the initial uniform deformation followed by localized necking, with significant grain growth in the necked region before final fracture of the specimen. This sample was strained at the strain rate $\dot{\varepsilon}\ \sim\ 1-2\ \times 10^{-4}\ \mathrm{s}^{-1}$ until failure with roughly one third of the specimen gauge in the view frame. Once localized width reduction occurs (Fig. 2d and e), increased grain growth is observed within that region, with grain sizes ranging up to 130 nm. This grain growth behavior accompanying neck formation was found to be general among all of the tested samples. That is, in cases where a neck developed, enhanced grain growth occurred within the necked region.

3.2. ACOM-based analysis of grain growth behavior

ACOM-based microstructure analysis provides a statistical route for revealing the average grain growth behavior accompanying deformation. Fig. 3 presents the before and after ACOM-based characterization of a sample deformed using the PTP device. Fig. 3a shows the clamped specimen on the device prior to the test. The specimen was loaded three separate times, with the stress-strain data for the first loading segment shown in Fig. 3d. From this curve, the apparent elastic modulus was calculated to be 25 GPa. The low elastic modulus (compared to bulk value around 70 GPa [49]), indicates an impact of Pt clamps on the measured sample compliance, which is not uncommon with PTP devices [50]. As the specimen is pulled, it is likely that a certain amount of slippage occurs between the Pt clamps and the Si chip. Fig. 3e shows the stress-strain curve for the final loading segment which concludes in specimen failure after an ultimate tensile stress of 575 MPa is reached. This specimen failed prior to necking due to crack propagation. Given the small dimensions of the specimens, morphological irregularities – such as edge roughness – can lead to significant stress concentrations and, in some instances, crack initiation prior to necking. The fractured specimen is shown at two different tilts in Fig. 3b,c. Significant plastic deformation resulted in specimen elongation and led to the buckling of

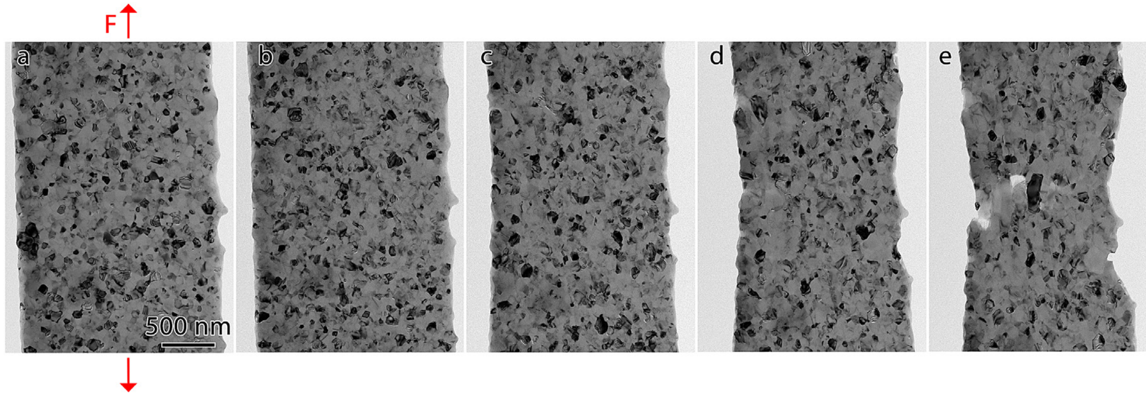

Fig. 2. Bright-field TEM images showing the microstructure evolution of a 200-nm-thick Al microspecimen under uniaxial load (direction of applied load indicated by red arrows). The frames taken at (a) 0%, (b) 4.7%, (c) 8.5%, (d) 12.1% and (e) 14.4% strain (For interpretation of the references to color in this figure legend, the reader is referred to the web version of this article.).

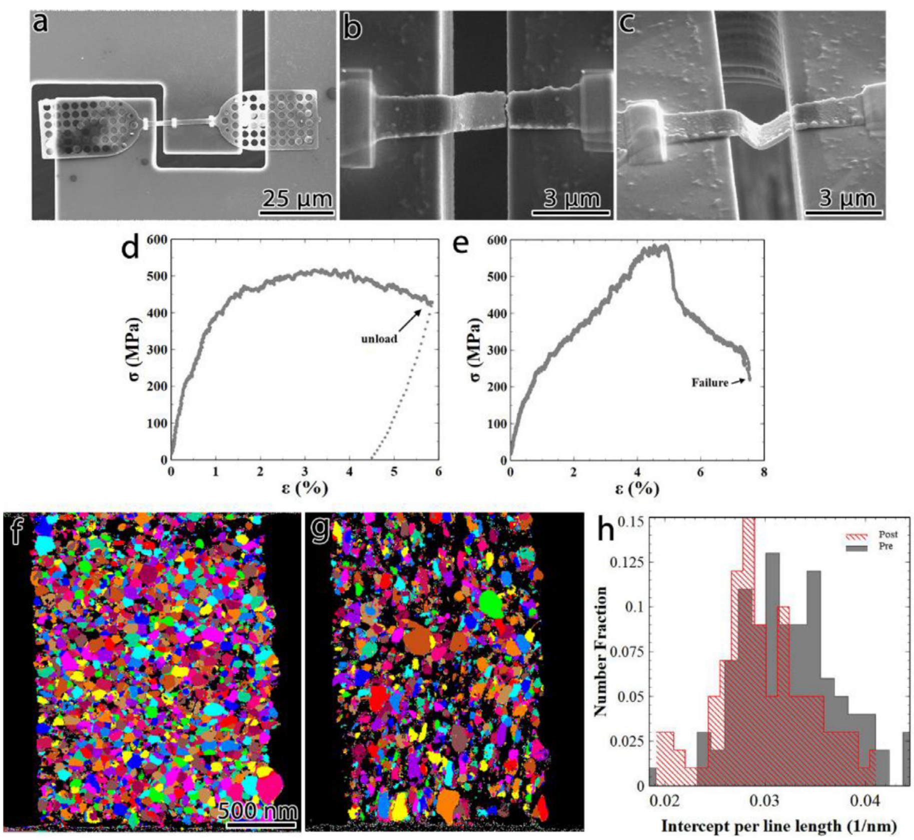

Fig. 3. *In situ* TEM PTP tensile test on Al specimen combined with ACOM. (a) Pre-test SEM image of specimen clamped on PTP device with Pt, (b) Post-test SEM image of fractured specimen, (c) tilted SEM image after failure showing extensive plastic deformation leading to bent specimen, (d) stress-strain curve for loading 1. After this loading segment, the load was removed. (e) stress-strain curve for the third loading for this specimen which resulted in failure. ACOM grain maps for (f) before testing began and (g) after failure and (h) corresponding grain size horizontal dimensions for pre-test (gray) and post-test (red-hatched) showing increased grain size post deformation.

the specimen upon unloading (Fig. 3c). Orientation unique color grain maps of the entire gauge length obtained by ACOM before testing and after failure are shown in Fig. 3f and g, respectively. Given that the fractured specimen is severely bent out-of-plane (Fig. 3c), fewer grains are able to be indexed for the fractured specimen (Fig. 3g). Despite this, it is clear that there is significant amount of grain growth for certain grains of the specimen. To quantify this, the grain size distribution was determined for the pre- and post-deformation ACOM maps using an intercept method, which measures the number of times a horizontal line of known length intersects with GBs. This method was specifically chosen due to the bent nature of the fractured specimen, as the vertical grain dimensions will be unreliable, while the horizontal dimensions are unaffected by the specimen angle. The results, presented in Fig. 3h, show the post-test data (red hatched) is shifted towards fewer intercepts when compared to the pre-test data (gray), indicating global grain growth has occurred during deformation. In addition, the horizontal dimensions of the largest of grains vary from 100 nm up to 180 nm, which is much larger than the starting grain size, indicating that grain growth has occurred. Overall, this experiment clearly demonstrates that grain growth occurs throughout the specimen, prior to neck formation. More detailed TEM analysis is provided in the next section.

3.3. Quantification of GB migration behavior

Fig. 4 is an example of the ability of the MEMS-based platform to capture real-time deformation while reliably measuring far-field stress and strain values. Data from this experiment are also shown in Figs. 5 to 7. The specimen was strained at $\dot{\varepsilon} \sim 3 \times 10^{-4}\ \mathrm{s}^{-1}$ until failure with roughly 45% of the specimen gauge in the view frame. Fig. 4a–f are TEM micrographs that track the deformation and formation of a neck. The view

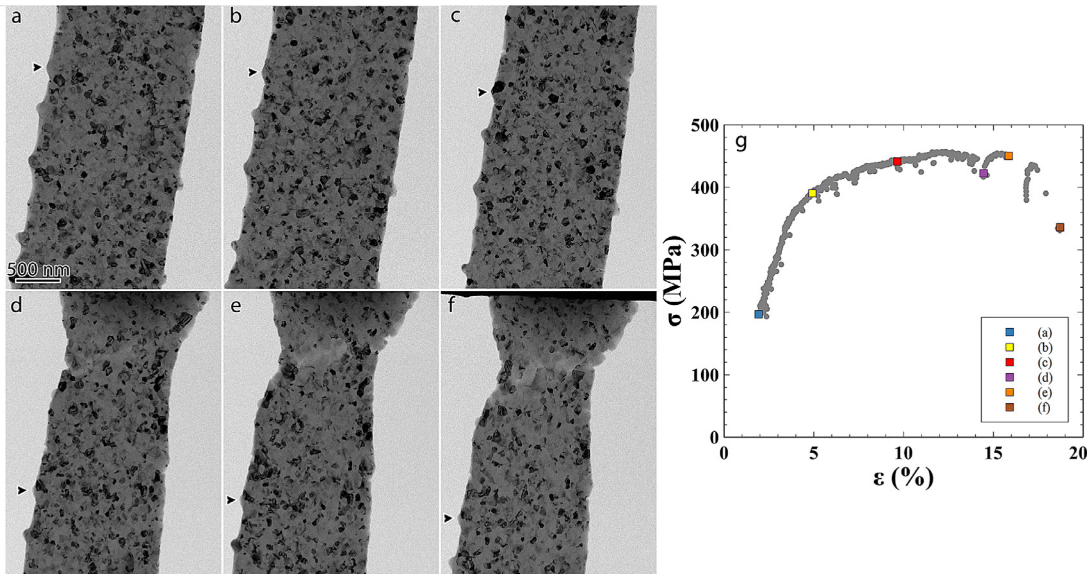

Fig. 4. Low magnification TEM images showing microstructure evolution at different strain values. The frames are taken at (a) 1.9%, (b) 4.9%, (c) 10%, (d) 14.5%, (d) 16.5% and (f) 18.7% total strain. Arrowhead in each designating the same feature. (g) Engineering stress-strain curve with the total strain of (a–f) indicated by the colored squares.

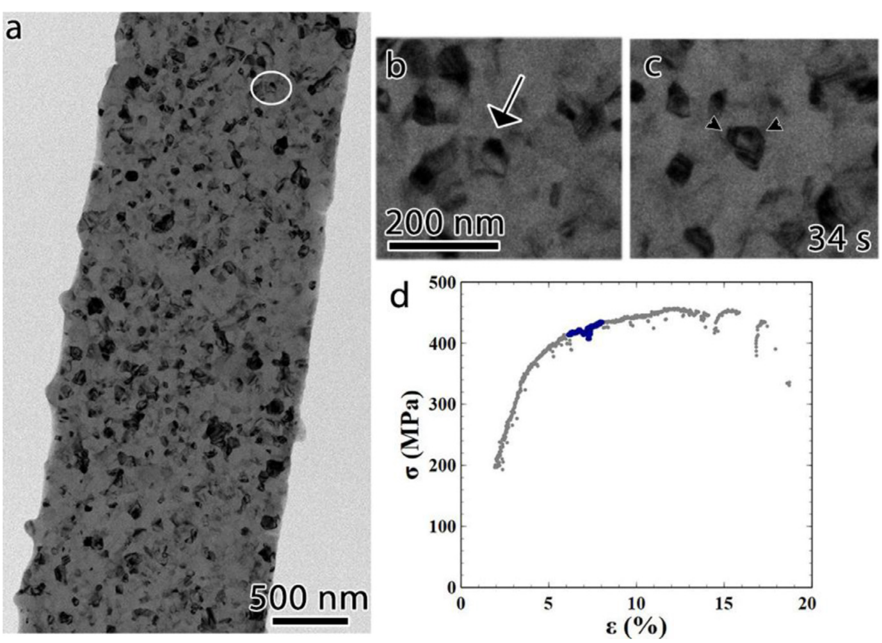

Fig. 5. GB migration during uniform deformation. (a) Low magnification TEM image showing no neck developed. Circle indicates location of grain marked by arrow in (b,c). (b) and (c) are digitally magnified snapshots taken 34 s apart during the highlighted portion in the stress-strain curve (d).

frame is moved towards the end to capture the neck, with the arrowhead marking the same location in each figure (Fig. 4d–f). The far-field engineering stress and strain values for each figure are marked in the accompanying stress-strain curve shown in Fig. 4g. From the data, the yield point and Young's modulus were determined to be 380 MPa and 8.9 GPa, respectively. The offset of the initial stress from a zero value results from residual tensile stress developing when the glue shrinks after curing (more details available in [45]). The low Young's modulus value stems from the approximate calculation of strain based on crosshead displacement values. The compliance of the glue leads to finite deformation of the thin film specimen along both the fillet region and the gauge section that is in contact with the glue (see Fig. 1c). These sections of the specimen are not included in the free-standing gauge length used to calculate strain, and therefore lead to an underestimate of Young's modulus [39]. While the measured value of Young's modulus is highly sensitive to the accuracy of small strain measurement, this issue does not affect the ability of the technique to measure relatively large plastic strains, as has been previously demonstrated [39,45]. The loading was paused twice in order to capture the neck formation in more detail, which resulted in the stress relaxation/drop seen prior to Fig. 4d (purple square in Fig. 4g) and after Fig. 4e (orange square in Fig. 4g). From the pre-test Fig. 4a to b, only minor contrast changes can be seen accompanied by a uniform reduction in width, with some contrast variations attributed to eliminating any film bending that might be present due to specimen manipulation. Continued width reduction is seen in the progression from Fig. 4b to c, however slight localized width reduction can be seen near the top of the micrograph. As deformation unfolds to Fig. 4d, localized reduction continues and leads to the development of a necked region.

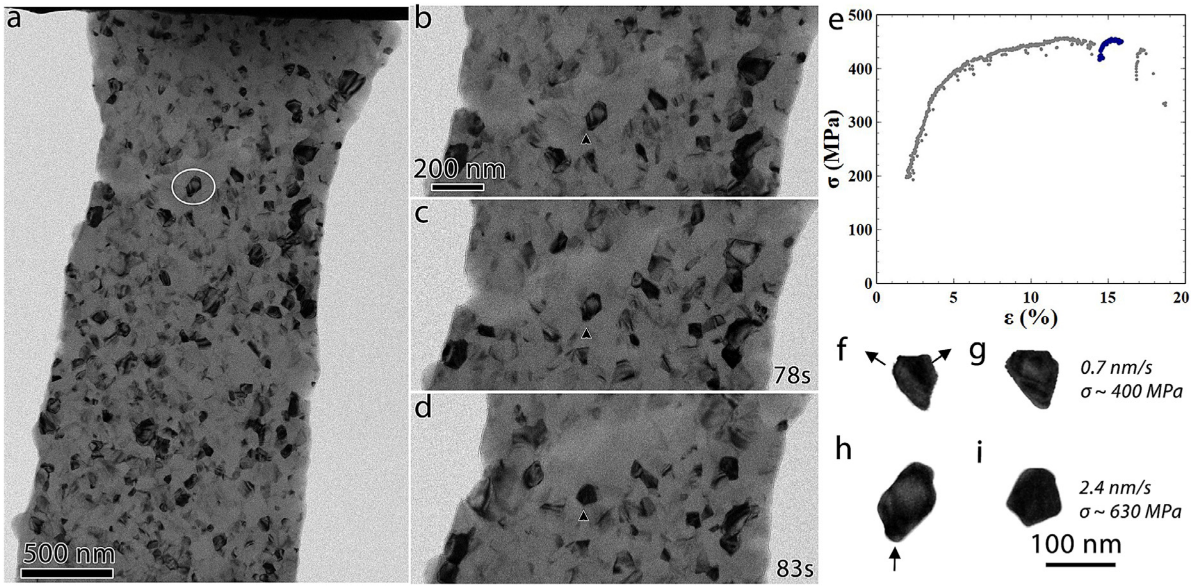

Fig. 6. Fast GB migration after neck develops. (a) Low magnification TEM image showing developed neck near top of snapshot. White circle indicates location of highlighted grain in (b–d). (e) Stress-strain curve with highlighted region corresponding to when snapshots (a-d) were recorded. Change in grain size as a function of time for (f,g) a grain in uniform region (from Fig. 5) and (h,i) necked region (from b–d). Arrows indicate direction of boundary migration. Both (g) and (i) are taken 5 s after (f) and (h), respectively. The size scale for both grains is the same and the respective GB migration velocities and estimated local stress are given.

The neck further develops in Fig. 4e and f where failure eventually occurs. Within this region, pronounced visible grain growth is observed, with grain sizes exceeding 250 nm.

In order to provide a further detailed view of the GB migration process, TEM video captured during the *in situ* deformation was analyzed to monitor when the onset of grain coarsening occurred and details of the grain growth process. Fig. 5 shows snapshots taken from a continuous video during the highlighted portion (dark blue segment) on the stress-strain curve (Fig. 5d), beginning at a far field plastic strain of 1.5% and stress of 415 MPa (see Suppl. Video 1). Fig. 5a is a low magnification snapshot illustrating that the specimen has undergone uniform elongation without the development of a necked region, with the white circle indicating the location of the grain of interest shown in Fig. 5b,c. At this point, the specimen is past yield but prior to reaching the ultimate tensile strength of 450 MPa and subsequent neck formation. The grain marked in Fig. 5b, with an equivalent diameter of 63 nm, undergoes grain growth over the course of 34 s, resulting in the grain shape shown in Fig. 5c and a final equivalent diameter of 75 nm (see Suppl. Video 2). The two GBs indicated by arrowheads in Fig. 5c migrated 17 nm at an average speed of 0.5 nm s^{-1} and a maximum 'jump' migration speed of 0.7 nm s^{-1} in direction normal to the respective GB. Contrast changes within the highlighted grain as well as in nearby grains could suggest that grain rotation accompanies the grain growth process. Interestingly, the highlighted region is where the neck eventually forms and appears to have increased amount of grain rotation compared to the remaining portion of the specimen, possibly indicating strain localization within this region occurs early in the deformation process and may be a required precursor to neck formation. Another example of boundary migration prior to necking is given in the Supplementary Information.

As deformation progresses and a neck develops, fast GB motion was observed within the necked region, with an example shown in Fig. 6. Fig. 6a shows that a neck has developed, and the corresponding stress has dropped below the ultimate tensile strength in Fig. 6e. (see Suppl. Video 4 for low-magnification observation of neck development). Resetting the TEM time $t = 0$, the vertical dimension of the grain marked by an arrowhead in Fig. 6b is measured at 115 nm. After 78 s, only a slight decrease to 112 nm occurs. However, from Fig. 6c to d, the bottom boundary migrates 12 nm in 5 s, resulting in a migration rate of 2.4 nm s^{-1} (see Suppl. Video 5). This indicates that within the necked region where the stresses are higher, boundary migration occurs at an increased speed resulting in the rapid collapsing of grains and by geometrical necessity, the rapid growth of neighboring grains. Within this region, the local gauge width is decreased from 1700 nm to 1190 nm. For a simple lower-bound estimate, this indicates that the local stress is increased by a factor of 1.4, resulting in a local stress of at least 630 MPa. This value is not accounting for any decrease in local film thickness that would also contribute to a further increase in stress. To better visualize the different migration rates, the grains traced in Figs. 5 and 6b–d have been isolated and shown in Fig. 6f,g and h,i, respectively. It is clear that the grain within the necked region experiences a larger change in grain size over the course of the 5 s separating Fig. 6h and i due to the faster GB migration speed of 2.4 nm s^{-1}. This is another example of 'jerky' type boundary motion, with limited motion for over a minute and then rapid boundary motion.

In order to quantitatively track grain growth further, grain sizes were measured using frames taken from TEM videos during the *in situ* deformation. The results of this analysis are shown in Fig. 7 by comparing measured grain size distributions within both the necked and uniform regions as the deformation progresses. Once a visible neck was formed, grain size was measured both within and outside the neck region and used to produce separate distributions. Fig. 7b shows an example of how the *necked* vs. *uniform* regions were defined: the grains within the two white lines were considered within the 'necked' region and grains outside that region were marked as within the 'uniform' region. The cumulative area fraction plots illustrate that grains within the necked region, represented by triangle markers and dashed lines, experience enhanced grain growth when compared to the uniform region (circle markers and solid lines) for the same strain value. For each strain value, there is a measurable increase in grain size within the necked region when compared to the uniform region. For ε = 14.1% (green data), half of the measured grains are below 94 nm within the uniform region, however, this value increases to 115 nm within the necked region. Measurable grain size increase within the necked region suggests that grain coarsening is caused by the increased stress, which is consistent with previous reports of stress-driven grain growth [18,21]. Additionally, there is little variation in grain size as the strain progresses within the 'uniform' re-

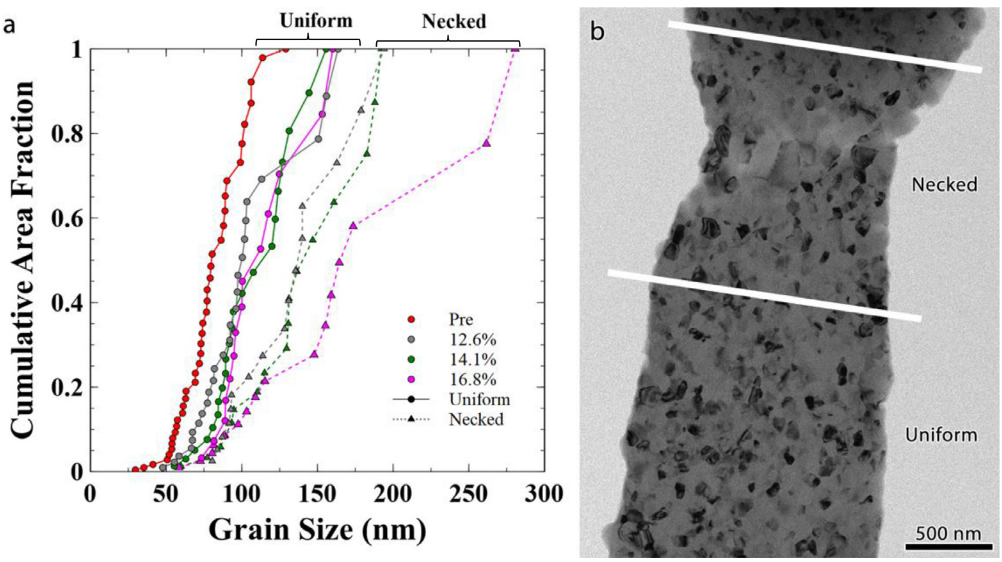

Fig. 7. (a) Cumulative area fraction grain size plots for different strain values post neck formation compared to the initial microstructure (red data). Data with circle markers and solid lines are taken from grains within the uniform region while data with triangle markers and dashed lines are from grains within the necked region. (b) Low magnification TEM micrograph designating regions defined as 'Necked' (in between white lines) and the remaining 'Uniform' region (For interpretation of the references to color in this figure legend, the reader is referred to the web version of this article.).

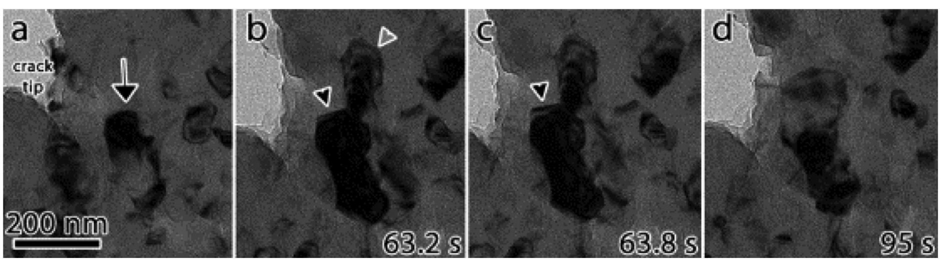

Fig. 8. Rapid GB motion ahead of crack tip. (a) the beginning of recorded segment. (b) $t = 63.2$ s, slight grain growth. (c) $t = 63.8$ s. Top boundary migrated 3.6 nm in the 0.6 s separating (b) and (c) resulting in migration speed of 6 nm s^{-1}. (d) $t = 95$ s, final grain structure prior to failure.

gion of the specimen. Within this region, the local stress is less than that within the necked region and thus likely not high enough to promote extensive grain coarsening. These results also suggest that the formation of a necked region further promotes grain coarsening. For example, the maximum grain size within the necked region for ε = 12.6% is 192 nm while for ε = 16.8%, the maximum is 280 nm. As deformation progresses and strain increases, the disparity between *uniform versus necked* region grain size increases as well. Each of the 'necked' data sets shares a similar grain size minimum of ~50 nm while the maximum grain size increase with strain. This is evidence of inhomogeneous grain growth as small grains remain, albeit with diminishing area fraction, while other grains grow resulting in increased maximum grain size.

Evidence presented thus far has pointed to GB migration promoted by increasing stress, and based on this, it would be expected that other sources of stress raisers would lead to a similar observation.

Fig. 8 shows such an example, where rapid GB migration is seen ahead of an extending crack tip during *in situ* TEM deformation (see Suppl. Video 6). In Fig. 8a, a relatively large grain with a vertical dimension of 268 nm in front of a crack tip is marked by an arrow. This dimension increases to 273.7 nm in Fig. 8b. Contrast changes in the above neighboring grain (marked with a gray arrowhead) indicate grain rotation. This could be associated with dislocation emission and absorption at GBs as well as rapid dislocation glide through the grain, although dislocations are not visible in the electron diffracting condition of the experiment. From Fig. 8b to c, the top boundary, marked by a black arrowhead, migrates upward 3.6 nm in 0.6 s, corresponding to a migration speed of 6 nm s^{-1}. The final grain microstructure, prior to complete failure, has a drastically increased vertical dimension of 336 nm, which is 1.25 times larger than the initial size as 268 nm. This is another example of the jerky, stop-and-go behavior of boundary migration, but with a GB migration rate 3–30 times larger than those measured in grains away from a crack tip.

During each of the above *in situ* TEM experiments, no dislocation activity is observed. However, post mortem TEM analysis shows dislocation structures present in the large grains near the fracture surfaces. One such example is seen in Fig. 9 and Suppl. Video 7. From Fig. 9a, it is clear that the fracture surface is intergranular and composed primarily of large grains, which is consistent with the previous analysis of pronounced grain growth within necked region. GB sliding is also seen to accompany the intergranular fracture (Suppl. Video 7). The fracture surface resembles a Wilsdorf-like tooth structure similar to previous reports [51,52]. An enlargement of the four highlighted grains (B, C, D and E) shows dark field images with evidence of intragranular dislocations, suggesting that either dislocation activity accompanies the grain growth process or dislocation activity initiates once the grains reach a critical size. These results are similar to those reported by Hattar et al. [53], which show that the density of both dislocations and deformation twins is much greater near the fractured surface than that of the gauge section in ufg Al thin films. Similarly, they reported intergranular crack propagation.

3.5. MD simulation results

Our MD simulations support *in situ* TEM observations of grain growth and further uncover the underlying atomic processes that are not directly visible through TEM. Fig. 10a and b show two views of the three-dimensional simulated nc Al thin film before tensile loading. In the x-y section view, Fig. 10b, four grains are labelled. These 4 grains and the associated GBs were traced during the MD simulation of tensile deformation. In Fig. 10a and b, the atomic configurations are colored by the common neighbor analysis in OVITO [54], so that the initial grain geometry and GB structures can be clearly visualized. Fig. 10c–f present a series of MD images at different tensile strains ε. In this work, an atom coloring scheme is developed and used to visualize both the initial GBs ($t = 0$) and current GBs (time t) in the same atomic configuration at

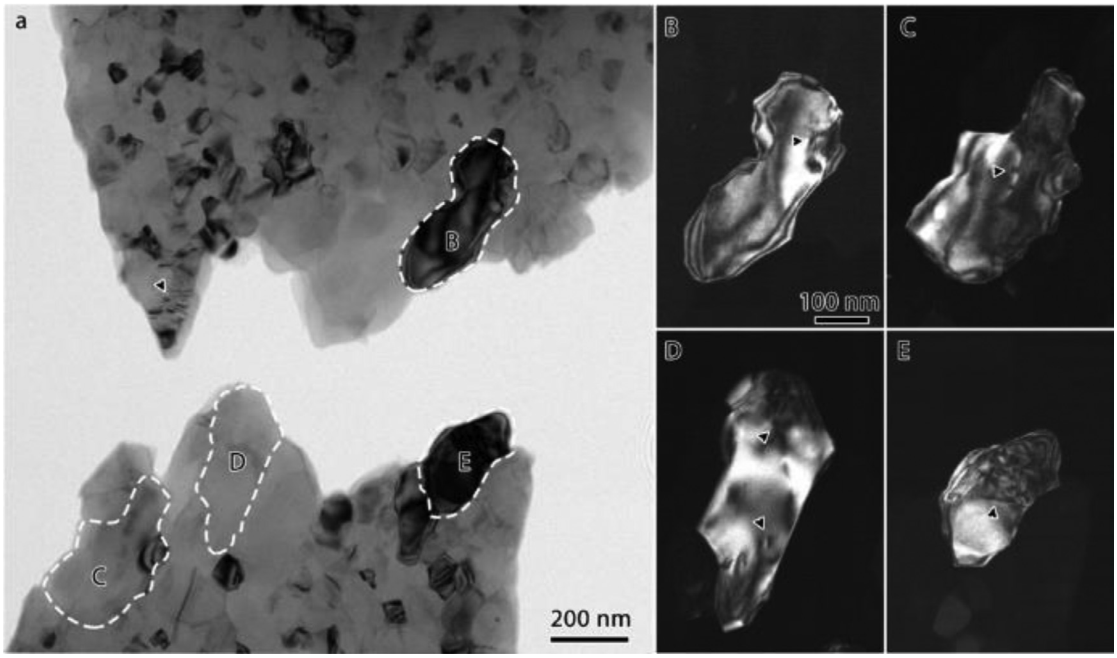

Fig. 9. Post mortem TEM analysis of fracture surface (a) multiple large grains near fracture surface, (b-e) enlarged dark-field TEM images of highlighted grains with evidence of dislocation structures indicated by arrowheads.

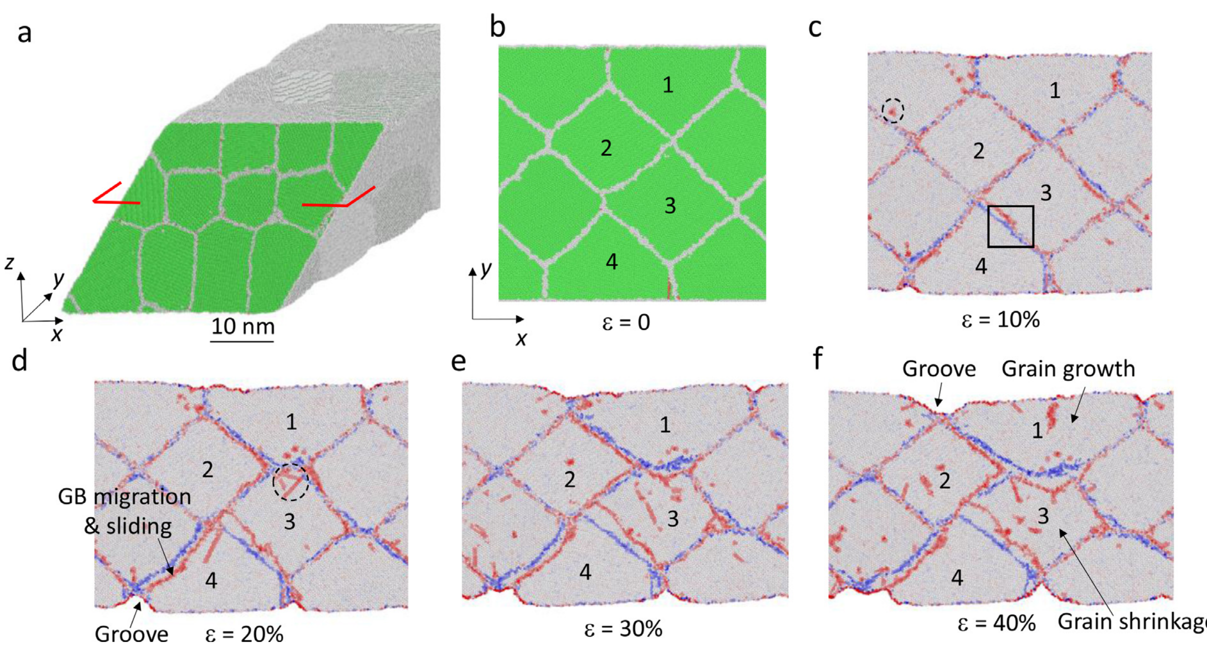

Fig. 10. MD simulation setup and results of small and modest plastic deformation during uniaxial tension of a nc Al thin film. (a) Three-dimensional view of the nc structure after annealing. Red segments indicate the cutting plane for exposing the x-y section of the film in (b). (b) Two-dimensional view of the x-y section of the film in (a). Atoms in (a-b) are colored by the common neighbor analysis in OVITO [54], showing atoms in GBs (light gray) and grain interiors (green). (c–f) MD snapshots at different applied tensile strains ε from 0 to 40%, showing the dislocation emission and absorption at GBs, GB migration and sliding, and grain growth and shrinkage. Atoms in (c–f) are colored by a scheme explained in the Supplementary Information such that both the initial GBs (at $t = 0$; with the constituent atoms colored in blue) and the current GBs (at time t; with the constituent atoms colored in red) are displayed in the same structure at time t; atoms in the stacking faults are colored in red; and other atoms are colored in light-gray (For interpretation of the references to color in this figure legend, the reader is referred to the web version of this article.).

time t. As described in detail in the Supplementary Information, this atom coloring scheme enables us to continuously trace the morphological evolution of grains and GBs, particularly GB migration, during tensile deformation of the nc thin film.

Close examination of the MD results (Fig. 10c–f and Suppl. Video 8) reveals the active mechanisms underlying our *in situ* TEM observations of plastic deformation and fracture in nc Al thin films. Throughout the MD simulations, dislocation activity is observed frequently. These dislocations usually emit from one side of GBs, traverse the grains, and are absorbed into the opposite side of GBs. Full dislocations of the $1/2\langle 110\rangle\{111\}$ type, which dissociate into leading and trailing partial dislocations of the $1/6\langle 112\rangle\{111\}$ type separated by narrow stacking fault regions, are the majority of intragranular lattice defects, consistent with the high stacking fault energy of Mishin et al. [48]. As these dislocations glide inside grains, Lomer-Cottrell locks (see circled examples in Fig. 10c and d) occasionally form, due to the intersection of two dislocations on different slip systems. These locks are disrupted as the applied load increases. The unlocked dislocations further glide inside grains and are eventually absorbed into GBs. Occasionally, only a leading partial is emitted from a GB, leaving behind a long stacking fault; the subsequent emission of a trailing partial occurs with increased load. For grains near the free surface, nucleation of surface dislocations is frequently observed, as the energy barrier of dislocation nucleation at the free surface is often lower than that in the bulk [55]. These MD results of deformation-induced dislocations of different types and on different slip systems complement our *in situ* TEM imaging that was taken along a specific orientation and thus revealed the activity of dislocations on certain slip systems.

In addition to dislocation activity, MD simulations reveal the active processes of GB migration and sliding. Because of random grain orientations, most GBs are of the mixed tilt and twist type. At $\varepsilon = 10\%$ (Fig. 10c), GB migration is clearly visible thanks to the aforementioned coloring scheme, which enables the display of both the initial and current GBs at the same time. It is seen from Fig. 10c that GB migration typically occurs at certain boundary segments and thus serves to accommodate local deformation incompatibilities between adjoining grains. GB migration is broadly distributed in different grains, thus facilitating an overall uniform elongation of the thin film. Coupled GB sliding and migration are often reported in previous MD simulations of sheared bicrystals [24]. However, our MD simulations reveal less active GB sliding than GB migration at small tensile strains (e.g., Fig. 10c at $\varepsilon = 10\%$), largely because of the geometrical constraints of grain triple junctions. We note that while the atom coloring scheme is effective for displaying GB migration, GB sliding is less obvious from the colored GBs, but can be determined by movements of grain triple junctions and GB intersections at the free surface.

As the applied tensile strain ε increases from 20 to 40% (Fig. 10d to f), GB migration gradually increases and also becomes increasingly non-uniform, resulting in large migration of several GBs. Compared to the triple junctions associated with interior GBs, the junctions between GBs and free surface are more prone to local reconstruction because of less surface constraints. As a result, the GBs intersecting the free surface often migrate much faster than the interior GBs. Migration of these near-surface GBs is often coupled with pronounced GB sliding, also because of the lack of surface constraints. Such GB sliding is evidenced by the formation of surface grooves, as seen in Fig. 10d to f. When grains are near the free surface, GB sliding will result in surface grooves as one surface grain will shift relative to the other. These MD results suggest that GB migration in the TEM thin film samples likely initiated from the film surface. As the applied tensile strain increases, the interior triple junctions are reconstructed, resulting in coupled GB sliding and migration. These highly active processes of GB migration and sliding result in drastic grain morphology changes, as evidenced by the growth of grain 1 and 4, and the concurrent shrinkage of grain 3 accompanied with a large shape change. The common occurrence of grain growth and shrinkage during MD is consistent with our *in situ* TEM observations. The change of grain 2 is relatively small, confirming the common occurrence of non-uniform grain deformation in polycrystalline materials, as revealed in the experimental data of grain size statistics in Fig. 7a. Incidentally, our MD simulations further reveal that coupled GB sliding and migration are primarily caused by glide of GB disconnections (to be discussed later), instead of less frequent dislocation emission and absorption at GBs that mainly serve to accommodate local deformation incompatibilities during GB migration.

The MD simulations further reveal the highly localized plastic deformation and final intergranular fracture in the nc Al thin film at large applied tensile strains. From a series of MD snapshots in Fig. 11 and Suppl. Video 8, it is seen that plastic deformation becomes increasingly localized in the region containing grains 1–4. Large migration of GB_{13} and GB_{34} causes drastic growth of grains 1 and 4 and shrinkage of grain 3, eventually resulting in direct contact between grains 1 and 4. Meanwhile, large sliding of GB_{12} and GB_{34} occurs, leading to growth of surface grooves associated with GB_{12} and GB_{34} (Fig. 11b). The increased stress concentrations in these deep grooves cause the continued slide-off of GB_{12} and GB_{34}, thereby producing the fractured surfaces of GB_{12} and GB_{34} (Fig. 11c). As the sliding-off of GB_{12} completes, the local fracture process switches to the sliding-off of GB_{34}. These processes demonstrate an intergranular fracture mode through large GB sliding, which is consistent with that observed during our *in situ* TEM testing of Al thin film samples. Hence, our MD results complement *in situ* TEM observations by revealing the atomic-level processes of GB sliding, leading to intergranular fracture in regions with large localized deformation.

5. Discussion

By utilizing *in situ* TEM straining techniques combined with MD simulations, we investigated deformation-induced grain growth in nc Al at room temperature. Deformation-induced grain growth has been observed in a multitude of studies, including tensile straining of nc Al [18,19,21], nc Ni [16], and nc Au [15] and under nanoindentation of nc Al [20,56] and nc Cu [22]. Some studies, however, report grain growth is preceded by grain rotation, suggesting that grain growth occurs by the coalescence of neighboring grains [15,16]. Direct evidence of GB migration in this study eliminates this as the dominant mechanism for grain growth. There is some evidence in this study to suggest grain rotation may occur prior to and after neck formation. However, we were unable to determine if the observed contrast changes were a direct result of crystallographic rotation due to dislocations passing through the grain or solely transgranular dislocation glide. In either case, the contrast changes are indicative of increased plastic deformation occurring within that region as it is not expected that global rotation of the specimen would result in bend contours within the local region.

The *in situ* observations in this work offer additional insight into the effect local stress has on GB migration. In the *in situ* experiments, extensive grain growth was observed to occur preferentially within the necked region of the specimens. The plot in Fig. 7a shows a clear relationship between grain size and the location on the specimen, *i.e.* grains were measured larger within the necked region *versus* grains within the uniform regions. This is strong evidence to suggest that the GB migration is driven by the local increase in stress within the necked region, which is also supported by our MD simulation results. Additionally, evidence that GB migration occurs outside of the necked region suggests that neck formation is not a direct result of grain growth but that instead, the increased stress within the necked region is necessary for increased GB migration. This is consistent with the growing number of studies that report stress-assisted GB migration leading to preferential grain growth in highly stressed regions [18,19,21,56–59]. To our knowledge, no other studies have related grain growth to the stress state imposed by a neck formation.

In this study, GB migration speeds varied from 0.2 – 0.7 nm s^{-1} for grains either outside or prior to neck formation (Figs. 5 and S1) when the applied tensile stresses were close to the ultimate tensile strength of 450 MPa. The GB migration speeds increased to 2.4 nm s^{-1} for grains within the necked region (Fig. 6) where the local tensile stresses were elevated to around 630 MPa, and even advanced to 6 nm s^{-1} for a growing grain ahead of a crack-tip (Fig. 8). The measured migration velocities are summarized in Table 1.

Other researchers have observed boundary migration speeds ranging of 5 – 10 nm s^{-1} for grains near a crack tip in pure nc Al down to 0.7 - 1 nm s^{-1} for boundaries doped with oxygen (impurities lead to a drag effect) [57]. Legros et al. has also reported speeds of 0.1 - 0.2 nm s^{-1} up to 50 and 200 nm s^{-1} for GB 'jumps' and suggested that these drastic speeds were a result of different mechanisms of migration [19]. The migration velocities reported in this study of 0.2 – 6 nm s^{-1} seem

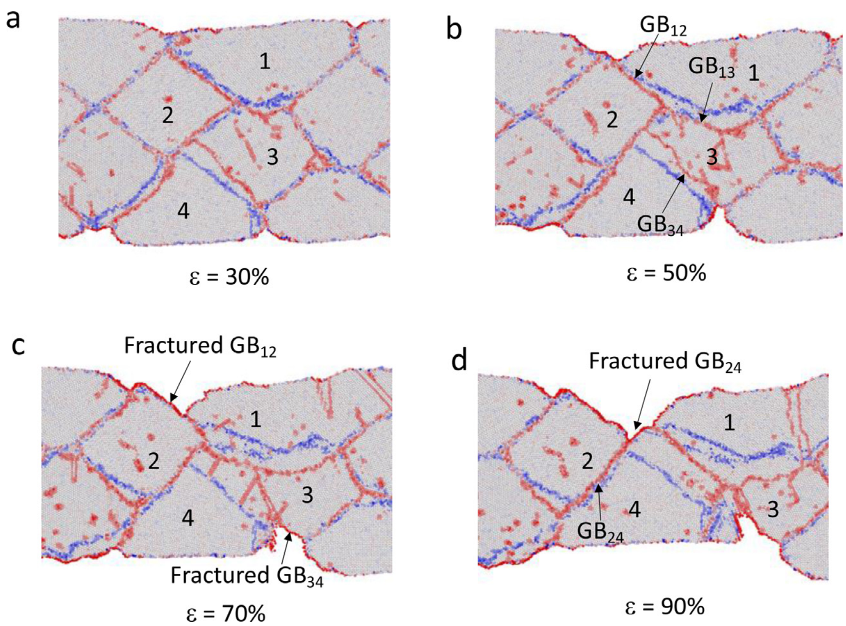

Fig. 11. MD simulation results of large plastic deformation and intergranular fracture during uniaxial tension of a nc Al thin film. (a–d) MD snapshots at different applied tensile strains ε from 30% to 90%, showing the drastic grain growth and shrinkage through large GB migration and sliding, as well as intergranular fracture via sliding-off of GBs. The same atom coloring scheme is used as in Fig. 10c–f.

Table 1
Measured grain boundary migration velocity for different grains from experiments on nanocrystalline Al thin films.

Grain location	Migration velocity (nm s^{-1})
Uniform	0.2
Uniform	0.7
Necked	2.4
Ahead of crack-tip	6

to be comparable with those reported in other studies as well as the 'jerky' migration behavior. The order of magnitude difference between the migration speed of grains prior to or outside neck formation and the grains within highly stressed regions likely reflect the inhomogeneity of driving force (stress) that can be measured by the present MEMS-based platform. Stress-driven GB migration is activated by stress and as such, areas of increased stress – such as within necked region or ahead of a growing crack – experience increased migration velocity. Other studies have suggested a similar trend by observing that grain size decreases with increasing distance from a crack tip and by geometrical necessity, GB migration velocity follows the same trend [19].

The general GBs in the current study are mostly of mixed tilt and twist type with high angle misorientation (Fig. 1f). As such, it is difficult to resolve the exact atomic mechanisms of GB migration through *in situ* TEM observations. However, our MD simulations offer atomistic insight into GB migration. Fig. 12 and Suppl. Video 9 show a representative example of stress-driven migration of a general GB between grain 3 and 4, denoted as GB_{34}, at the applied tensile strain $\varepsilon = 10\%$; this GB segment is boxed in Fig. 10c. The atomic structure of GB_{34} is viewed along the $\langle 110 \rangle$ direction of grain 3, thereby showing a clear image of projected $\langle 110 \rangle$ atomic columns inside this grain. Since GB_{34} is of mixed tilt and twist type, grain 4 is not aligned with a specific crystallographic direction, such that the projected atomic columns overlap with each other in grain 4. The contrast of projected atomic columns in the adjoining grain 3 and 4 facilitates our tracking of the atomically sharp GB_{34} during its migration. Note that GB_{34} consists of atomic-sized boundary steps on the edge-on $\{111\}$ planes in grain 3. By comparing local GB steps (marked by blue lines) relative to a reference $\{111\}$ plane marked by the red dashed line, it is seen from Fig. 12a–c that migration of GB_{34} towards grain 3 occurs through glide of GB steps. In general, a GB disconnection consists of both a GB step and a GB dislocation component. For a GB of mixed tilt and twist type, the observed gliding of a GB step signals the movement of a corresponding GB disconnection, while the GB dislocation component cannot be easily visualized due to complex lattice geometry but usually moves simultaneously with the GB step. Hence, MD results in Fig. 12 complement our *in situ* TEM observations by revealing the representative atomic-scale processes of coupled GB sliding and migration through gliding of disconnections on a general GB in nc Al.

Despite differences in strain rate, grain morphology and film dimensions between MD simulations and experiments, qualitative agreement was found in the GB migration and fracture behavior, which was found most pronounced in areas with localized necking deformation. Both simulations and experimental results point to GB migration leading to grain growth as a dominant deformation mechanism. The MD simulations suggest that dislocation emission and absorption are not a major contributor to the migration and sliding but do play a role in accommodating deformation incompatibility at GBs. This is consistent with experimental findings that showed *in situ* evidence of bend contours (suggestive of dislocation activity) and post mortem observations of dislocation structures, but that GB migration was also observed to occur separate from dislocation evidence. Bend contours can be indicative of dislocation activity as the glide of countless dislocations can lead to a change in grain orientation which can cause bend contours. Both simulations and experiments also show that GB migration begins early in deformation and is further promoted by increased stress due to localized deformation (necking or surface grooves). As with the experimental results, the simulations also show inhomogeneous grain growth with certain grains growing at the expense of other. Additionally, MD simulations reveal the atomic-scale processes of coupled GB sliding and migration through gliding of GB disconnections. Finally, large GB sliding is observed in both simulations and experiments (especially near fracture surface). This GB sliding was found to lead to intergranular fracture as the observed failure mechanism.

6. Conclusion

Using *in situ* TEM MEMS-based straining combined with MD simulations, we have studied deformation-induced grain growth while also investigating how the local stress imposed by necking promotes GB migration. The results of these experiments indicate that GB migration is primarily stress-induced, as opposed to thermally-driven GB migra-

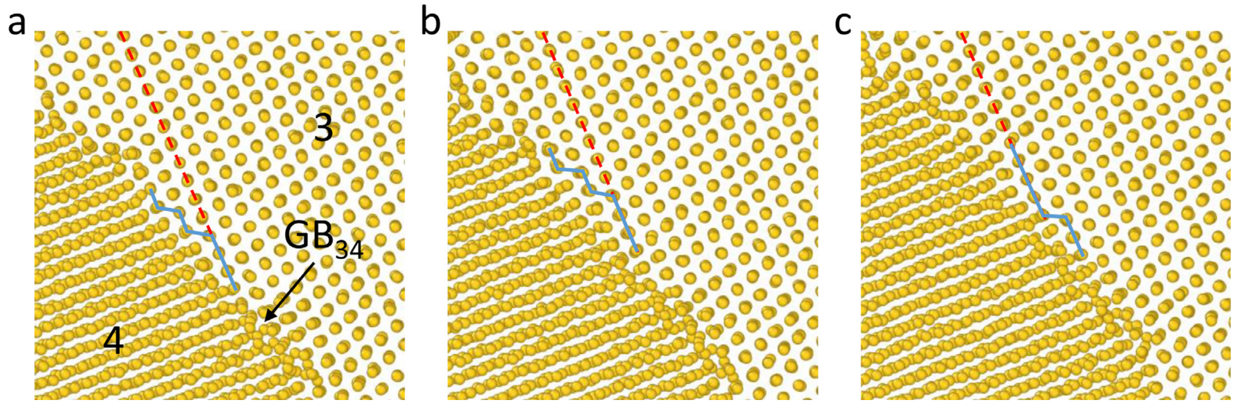

Fig. 12. MD results showing atomic-scale processes of migration of a general GB of mixed tilt and twist type in nc Al. (a–c) MD snapshots of migration of GB_{34} toward grain 3 through the glide of GB steps (indicated by blue lines), signaling the glide of corresponding GB disconnections. This GB corresponds to the boxed region of GB_{34} in Fig. 10c at 10% strain. The atomic configuration is viewed along the ⟨110⟩ direction of grain 3. The red dashed line indicates the edge-on {111} plane in grain 3.

tion during high temperature annealing or creep. The local increase in stress (either due to necking or a crack tip) drives faster GB migration. Measured GB migration speeds ranged from 0.2 – 0.7 nm s^{-1} when the applied tensile stresses were close to the ultimate tensile strength of 450 MPa, increased up to 2.5 nm s^{-1} for grains within the necked region where the local tensile stresses were elevated to around 630 MPa, and even rose to 6 nm s^{-1} for GB migration that occurred ahead of crack tip. MD simulations utilized a coloring scheme to easily track GB motion over time, which yielded qualitative agreement with experimental observations that significant GB migration leads to grain growth. MD simulations further complement *in situ* experiments by uncovering the underlying atomic processes of grain growth, GB migration and intergranular fracture that are not directly visible through TEM. Altogether, these results underscore the important role of stress-driven grain growth in plastically deforming nanocrystalline metals, particularly in regions with large localized deformation.

Declaration of Competing Interest

The authors declare that they have no known competing financial interests or personal relationships that could have appeared to influence the work reported in this paper.

Acknowledgments

SS, YZ, OP, TZ, and JK gratefully acknowledge support by the U.S. Department of Energy (DOE), Office of Science, Basic Energy Sciences (BES) Materials Science and Engineering (MSE) Division under Award #DE-SC0018960. S.S. is also supported by the U.S. Department of Energy (DOE) National Nuclear Security Administration (NNSA) Stewardship Science Graduate Fellowship (SSGF) program, provided under cooperative agreement number DE-NA0003960. C.M.B and K.H. time was also supported support by the U.S. Department of Energy (DOE), Office of Science, Basic Energy Sciences (BES) Materials Science and Engineering (MSE) Division, but under Award #15013170. This work was performed, in part, at the Center for Integrated Nanotechnologies, an Office of Science User Facility operated for the U.S. Department of Energy (DOE) Office of Science. Sandia National Laboratories is a multimission laboratory managed and operated by National Technology & Engineering Solutions of Sandia, LLC, a wholly owned subsidiary of Honeywell International, Inc., for the U.S. DOE's National Nuclear Security Administration under contract DE-NA-0003525. The views expressed in the article do not necessarily represent the views of the U.S. DOE or the United States Government.

Supplementary materials

Supplementary material associated with this article can be found, in the online version, at doi:10.1016/j.mtla.2021.101068.

References

[1] M.A. Meyers, A. Mishra, D.J. Benson, Mechanical properties of nanocrystalline materials, Prog. Mater. Sci. 51 (2006) 427–556.
[2] E.O. Hall, The deformation and ageing of mild steel: II characteristics of the Lüders deformation, Proc. Phys. Soc. Sect. B 64 (1951) 747–753.
[3] N.J. Petch, The cleavage strength of polycrystals, J. Iron Steel Inst. 174 (1953) 25–28.
[4] P.G. Sanders, J.A. Eastman, J.R. Weertman, Elastic and tensile behavior of nanocrystalline copper and palladium, Acta Mater. 45 (1997) 4019–4025.
[5] G.W. Nieman, J.R. Weertman, R.W. Siegel, Mechanical behavior of nanocrystalline Cu and Pd, J. Mater. Res. 6 (1991) 1012–1027.
[6] H. Conrad, Plastic deformation kinetics in nanocrystalline FCC metals based on the pile-up of dislocations, Nanotechnology 18 (2007) 325701.
[7] E. Arzt, Size effects in materials due to microstructural and dimensional constraints: A comparative review, Acta Mater. 46 (1998) 5611–5626.
[8] T.G. Nieh, J. Wadsworth, Hall-petch relation in nanocrystalline solids, Scr. Mater. 25 (1991) 955–958.
[9] H. Van Swygenhoven, P.M. Derlet, Grain-boundary sliding in nanocrystalline fcc metals, Phys. Rev. B 64 (2001) 224105.
[10] H. Van Swygenhoven, M. Spaczer, A. Caro, D. Farkas, Competing plastic deformation mechanisms in nanophase metals, Phys. Rev. B 60 (1999) 22–25.
[11] H. Van Swygenhoven, P.M. Derlet, A. Hasnaoui, Atomic mechanism for dislocation emission from nanosized grain boundaries, Phys. Rev. B 66 (2002) 024101.
[12] J. Schioøtz, K.W. Jacobsen, A maximum in the strength of nanocrystalline copper, Science 301 (2003) 1357–1359.
[13] E. Izadi, A. Darbal, R. Sarkar, J. Rajagopalan, Grain rotations in ultrafine-grained aluminum films studied using *in situ* TEM straining with automated crystal orientation mapping, Mater. Des. 113 (2017) 186–194.
[14] H. Idrissi, A. Kobler, B. Amin-Ahmadi, M. Coulombier, M. Galceran, J.P. Raskin, S. Godet, C. Kübel, T. Pardoen, D. Schryvers, Plasticity mechanisms in ultrafine grained freestanding aluminum thin films revealed by *in-situ* transmission electron microscopy nanomechanical testing, Appl. Phys. Lett. 104 (2014) 081906.
[15] A. Kobler, A. Kashiwar, H. Hahn, C. Kübel, Combination of *in situ* straining and ACOM TEM: a novel method for analysis of plastic deformation of nanocrystalline metals, Ultramicroscopy 128 (2013) 68–81.
[16] Y.B. Wang, B.Q. Li, M.L. Sui, S.X. Mao, Deformation-induced grain rotation and growth in nanocrystalline Ni, Appl. Phys. Lett. 92 (2008) 061921.
[17] R.L. Coble, A model for boundary diffusion controlled creep in polycrystalline materials, J. Appl. Phys. 34 (1963) 1679–1682.
[18] D.S. Gianola, S. Van Petegem, M. Legros, S. Brandstetter, H. Van Swygenhoven, K.J. Hemker, Stress-assisted discontinuous grain growth and its effect on the deformation behavior of nanycrystalline aluminum thin films, Acta Mater. 54 (2006) 2253–2263.
[19] M. Legros, D.S. Gianola, K.J. Hemker, *In situ* TEM observations of fast grain-boundary motion in stressed nanocrystalline aluminum films, Acta Mater. 56 (2008) 3380–3393.
[20] M. Jin, A.M. Minor, J.W. Morris, Strain-induced coarsening in nano-grained films, Thin Solid Film 515 (2007) 3202–3207.
[21] T.J. Rupert, D.S. Gianola, Y. Gan, K.J. Hemker, Experimental observations of stress–driven grain boundary migration, Science 326 (2009) 1686–1690.

[22] K. Zhang, J.R. Weertman, J.A. Eastman, Rapid stress-driven grain coarsening in nanocrystalline Cu at ambient and cryogenic temperatures, Appl. Phys. Lett. 87 (2005) 061921.
[23] W.T. Read, W. Shockley, Dislocation models of crystal grain boundaries, Phys. Rev. 78 (1950) 275–289.
[24] J.W. Cahn, Y. Mishin, A. Suzuki, Coupling grain boundary motion to shear deformation, Acta Mater. 54 (2006) 4953–4975.
[25] J. Han, S.L. Thomas, D.J. Srolovitz, Grain-boundary kinetics: a unified approach, Prog. Mater. Sci. 98 (2018) 386–476.
[26] A. Suzuki, Y.M. Mishin, Atomic mechanisms of grain boundary motion, Mater. Sci. Forum 502 (2005) 157–162.
[27] M. Winning, G. Gottstein, L.S. Shvindlerman, On the mechanisms of grain boundary migration, Acta Mater. 50 (2002) 353–363.
[28] G. Gottstein, D.A. Molodov, L.S. Shvindlerman, D.J. Srolovitz, M. Winning, Grain boundary migration: Misorientation dependence, Solid State Mater. Sci. 5 (2001) 9–14.
[29] J.W. Cahn, Y. Mishin, A. Suzuki, Duality of dislocation content of grain boundaries, Philos. Mag. 86 (2006) 3965–3980.
[30] A.H. King, D.A. Smith, The effects on grain-boundary processes of the steps in the boundary plane associated with the cores of grain-boundary dislocations, Acta Crystallogr. Sect. A 36 (1980) 335–343.
[31] C.M.F. Rae, D.A. Smith, On the mechanisms of grain boundary migration, Philos. Mag. A 41 (1980) 477–492.
[32] H. Fukutomi, T. Kamijo, Grain boundary sliding-migration of aluminum $<110>$ Σ11 {113} symmetric tilt coincidence grain boundary and its interpretation based on the motion of perfect DSC dislocations, Scr. Metall. 19 (1985) 195–197.
[33] K.L. Merkle, L.J. Thompson, F. Phillipp, *In-situ* HREM studies of grain boundary migration, Interface Sci. 12 (2004) 277–292.
[34] Q. Zhu, G. Cao, J. Wang, C. Deng, J. Li, Z. Zhang, S.X. Mao, *In situ* atomistic observation of disconnection-mediated grain boundary migration, Nat. Commun. 10 (2019) 156.
[35] A. Rajabzadeh, M. Legros, N. Combe, F. Mompiou, D.A. Molodov, Evidence of grain boundary dislocation step motion associated to shear-coupled grain boundary migration, Philos. Mag. 93 (2013) 1299–1316.
[36] N. Tsuji, Y. Ito, Y. Saito, Y. Minamino, Strength and ductility of ultrafine grained aluminum and iron produced by ARB and annealing, Scr. Mater. 47 (2002) 893–899.
[37] E. Bruder, Formability of ultrafine grained metals produced by severe plastic deformation–an overview, Adv. Eng. Mater. 21 (2019) 1800316.
[38] E. Hosseinian, O.N. Pierron, Quantitative *in situ* TEM tensile fatigue testing on nanocrystalline metallic ultrathin films, Nanoscale 5 (2013) 12532–12541.
[39] S. Gupta, O.N. Pierron, A MEMS tensile testing technique for measuring true activation volume and effective stress in nanocrystalline ultrathin microbeams, Microelectromech. Syst. 26 (2017) 1082–1092.
[40] S. Gupta, O.N. Pierron, MEMS based nanomechanical testing method with independent electronic sensing of stress and strain, Extrem. Mech. Lett. 8 (2016) 167–176.
[41] B. Pant, B.L. Allen, T. Zhu, K. Gall, O.N. Pierron, A versatile microelectromechanical system for nanomechanical testing, Appl. Phys. Lett. 98 (2011) 053506.
[42] B. Pant, S. Choi, E. Baumert, B.L. Allen, S. Graham, K. Gall, O.N. Pierron, MEMS-based nanomechanics: influence of MEMS design on test temperature, Exp. Mech. 52 (2012) 607–617.
[43] E. Hosseinian, S. Gupta, O.N. Pierron, M. Legros, Size effects on intergranular crack growth mechanisms in ultrathin nanocrystalline gold free-standing films, Acta Mater. 143 (2018) 77–87.
[44] E. Hosseinian, M. Legros, O.N. Pierron, Quantifying and observing viscoplasticity at the nanoscale: highly localized deformation mechanisms in ultrathin nanocrystalline gold films, Nanoscale 8 (2016) 9234–9244.
[45] S. Gupta, S. Stangebye, K. Jungjohann, B. Boyce, T. Zhu, J. Kacher, O.N. Pierron, *In situ* TEM measurement of activation volume in ultrafine grained gold, Nanoscale 12 (2020) 7146–7158.
[46] R. Sarkar, C. Rentenberger, J. Rajagopalan, Electron beam induced artifacts during *in situ* TEM deformation of nanostructured metals, Sci. Rep. 5 (2015) 1–11.
[47] S. Plimpton, Fast parallel algorithms for short-range molecular dynamics, J. Comput. Phys. 117 (1995) 1–19.
[48] Y. Mishin, D. Farkas, M.J. Mehl, D.A. Papaconstantopoulos, Interatomic potentials for monoatomic metals from experimental data and ab initio calculations, Phys. Rev. B 59 (1999) 3393–3407.
[49] H. Li, X. Dong, Y. Shen, A. Diehl, H. Hagenah, U. Engel, M. Merklein, Size effect on springback behavior due to plastic strain gradient hardening in microbending process of pure aluminum foils, Mater. Sci. Eng. A 527 (2010) 4497–4504.
[50] C. Chisholm, H. Bei, M.B. Lowry, J. Oh, S.A.S. Asif, O.L. Warren, Z.W. Shan, E.P. George, A.M. Minor, Dislocation starvation and exhaustion hardening in Mo alloy nanofibers, Acta Mater. 60 (2012) 2258–2264.
[51] H.G.F. Wilsdorf, The role of glide and twinning in the final separation of ruptured gold crystals, Acta Metall. 30 (1982) 1247–1258.
[52] H.G.F. Wilsdorf, The ductile fracture of metals:a microstructural viewpoint, Mater. Sci. Eng. 59 (1983) 1–39.
[53] K. Hattar, J. Han, M.T.A. Saif, I.M. Robertson, *In situ* transmission electron microscopy observations of toughening mechanisms in ultra-fine grained columnar aluminum thin films, J. Mater. Res. 20 (2005) 1869–1877, doi:10.1557/JMR.2005.0233.
[54] A. Stukowski, Visualization and analysis of atomistic simulation data with OVITO-the open visualization tool, Model. Simul. Mater. Sci. Eng. 18 (2010) 015012.
[55] T. Zhu, J. Li, A. Samanta, A. Leach, K. Gall, Temperature and strain-rate dependence of surface dislocation nucleation, Phys. Rev. Lett. 100 (2008) 025502.
[56] M. Jin, A.M. Minor, E.A. Stach, J.W. Morris Jr., Direct observation of deformation-induced grain growth during nanoindentation of ultrafine-grained Al at room temperature, Acta Mater. 52 (2004) 5381–5387.
[57] M. He, S. Samudrala, G. Kim, P. Felfer, A. Breen, J. Cairney, D. Gianola, Linking stress-driven microstructural evolution in nanocrystalline aluminium with grain boundary doping of oxygen, Nat. Commun. 7 (2016) 11225.
[58] F. Mompiou, M. Legros, A. Boé, M. Coulombier, J.P. Raskin, T. Pardoen, Inter- and intragranular plasticity mechanisms in ultrafine-grained Al thin films: an *in situ* TEM study, Acta Mater. 61 (2013) 205–216.
[59] T.A. Furnish, B.L. Boyce, J.A. Sharon, C.J. O'Brien, B.G. Clark, C.L. Arrington, J.R. Pillars, Fatigue stress concentration and notch sensitivity in nanocrystalline metals, J. Mater. Res. 31 (2016) 740–752.